Materials and Design 199 (2021) 109400

Contents lists available at ScienceDirect

Materials and Design

journal homepage: www.elsevier.com/locate/matdes

Characterization, mechanical properties and dimensional accuracy of a Zr-based bulk metallic glass manufactured via laser powder-bed fusion

Navid Sohrabi [a,*], Jamasp Jhabvala [a], Güven Kurtuldu [b], Mihai Stoica [b], Annapaola Parrilli [c], Siddartha Berns [d], Efthymios Polatidis [e], Steven Van Petegem [f], Sylvain Hugon [d], Antonia Neels [c], Jörg F. Löffler [b], Roland E. Logé [a]

[a] Thermomechanical Metallurgy Laboratory, PX Group Chair, Ecole Polytechnique Fédérale de Lausanne (EPFL), 2002 Neuchâtel, Switzerland
[b] Laboratory of Metal Physics and Technology, Department of Materials, ETH Zurich, 8093 Zurich, Switzerland
[c] Center for X-ray Analytics, Swiss Federal Laboratories for Materials Science and Technology (Empa), 8600 Dübendorf, Switzerland
[d] COMATEC HEIG-VD, 1400 Yverdon-les-Bains, Switzerland
[e] Laboratory for Neutron Scattering and Imaging, Paul Scherrer Institute, 5232 Villingen-PSI, Switzerland
[f] Photons for Engineering and Manufacturing, Paul Scherrer Institute, 5232 Villingen-PSI, Switzerland

HIGHLIGHTS

- Advanced characterization is required to detect nanocrystals formed during the Laser powder-bed fusion process
- Results of finite element simulation and fast differential scanning calorimetry unveil the mechanism of crystallization
- Despite the presence of nanocrystals in the Zr-based BMG, excellent mechanical properties are achieved
- Using optimized parameters, a benchmark with complex features is fabricated with excellent geometrical accuracy

GRAPHICAL ABSTRACT

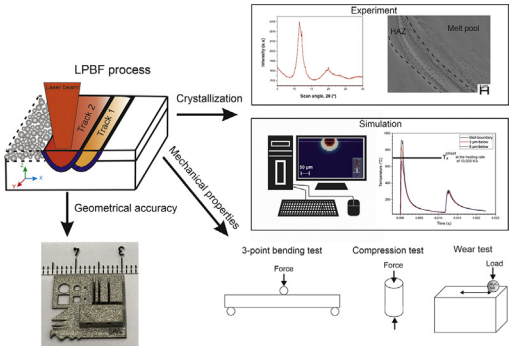

ARTICLE INFO

Article history:
Received 7 November 2020
Received in revised form 26 November 2020
Accepted 8 December 2020
Available online 10 December 2020

Keywords:
Additive manufacturing
Bulk metallic glass
Laser powder-bed fusion
Nano-crystallization
Precision manufacturing
Selective laser melting

ABSTRACT

Bulk metallic glasses (BMGs) are high-strength, highly elastic materials due to their disordered atomic structure. Because BMGs require sufficiently high cooling rates to bypass crystallization, laser-based additive manufacturing (AM) methods have recently been employed for the fabrication of BMGs. In this study, we present an optimized Laser Powder-Bed Fusion (LPBF) process on a Zr-based BMG ($Zr_{59.3}Cu_{28.8}Al_{10.4}Nb_{1.5}$, in at.%), with a focus on characterization, mechanical properties, and dimensional accuracy. A volumetric density of 99.82% was achieved. Although the sample was qualified as amorphous via laboratory X-ray diffraction experiments, a more meticulous study using synchrotron radiation revealed nanocrystals in the heat-affected zones (HAZs) of the melt pool. Fast differential scanning calorimetry (FDSC) and numerical simulations were then employed to illustrate the mechanism of crystallization. The LPBF-processed alloy revealed excellent mechanical properties, such as high hardness, wear resistance, compressive strength, and flexural strength. Apart from vein-like patterns, the fracture surfaces of the compression test samples showed liquid-like features, which indicate a significant local temperature increase during fracture. The dimensional accuracy was assessed with a benchmark exhibiting complex geometrical features and reached at least 40 μm. The results indicate that LPBF processing is a promising route for the manufacturing of BMGs for various applications.

* Corresponding author.
E-mail address: navid.sohrabi@epfl.ch (N. Sohrabi).

https://doi.org/10.1016/j.matdes.2020.109400

1. Introduction

Bulk Metallic Glasses (BMGs) are known for their excellent mechanical properties, provided they retain the amorphous structure inherited from a sufficiently high cooling rate from the melt. Due to the lack of defects such as grain boundaries and dislocations, BMGs possess high hardness and strength, excellent wear resistance, and a high elastic limit, usually combined with a low Young's modulus. Applications range from jewelry to electronics and sports goods [1–5]. One of the main drawbacks of BMGs' conventional production methods, such as casting and melt spinning, is the size limit and the restriction to simple shapes [6]. When the size of the cast sample exceeds the so-called critical casting diameter of the alloy, crystallization is initiated, which generally has an adverse effect on the mechanical properties. The widespread use of BMGs in industry is thus limited by the lack of possibility to manufacture large BMG samples with complex shapes [7,8].

Recently, laser-based additive manufacturing (AM) methods have been used to produce BMGs via the high cooling rate provided by laser processing [9]. The mostly used AM method has been Laser Powder-Bed Fusion (LPBF), and various BMGs based on Fe [10–19], Al [20–23], Zr [24–40], Ti [41], and Cu [42,43] have been printed by LPBF. In fact, LPBF has several advantages over conventional manufacturing methods, such as the possibility to build parts with complicated geometries, minimal feedstock waste and no size limitation [44]. Since the interaction between the laser and the deposited powder is short and confined to a small volume, the local cooling rate (R_c) can reach 10^3–10^8 K/s [9], which is typically higher than the critical cooling rate (CR_c) of most BMGs [45,46]. Mahbooba et al. [14] printed a Fe-based BMG sample via LPBF, which was 15 times larger in all dimensions than the critical casting diameter. Despite the very high cooling rates in LPBF, partial crystallization remains difficult to avoid. Studies on LPBF of Zr-based BMGs [24,35–39,], Fe-based BMGs [11,13,14], Al-based BMGs [20–23], and Cu-based BMGs [42,43] reported the occurrence of crystallization, and presented various explanations for the crystallization of BMGs during the LPBF process. Li et al. [24] suggested that chemical heterogeneities in the melt pool cause crystallization, while Ouyang et al. [35] suggested that the time that the material experiences in the HAZ above the crystallization temperature is the decisive factor for crystallization. Lu et al. [42] studied LPBF of a Cu-based BMG and illustrated that structural relaxation due to the cyclic nature of the LPBF process may cause crystallization. Lindwall et al. [47] reported on an increase of temperature as the number of layers increases and consequently on a decrease in cooling rate that generates crystallization.

Most of the studies on LPBF of BMGs have focused on the optimization of the processing parameters and the possibility of producing amorphous parts [13,14,24,33,39]. Less attention has been paid to their mechanical properties. While the most-reported physical quantity was the hardness of the LPBF-processed BMGs, other tests were only found in a few studies. Zhang et al. [27] fabricated a partially crystalline Zr-based BMG with a density of 99.7% for biomedical applications. They reported a wear resistance lower than that of Ti-6Al-4 V, commonly used for the same application. Although hardness and compressive strength were similar to those of as-cast samples, fracture toughness was reduced by half. The discrepancy was attributed to the low toughness in the HAZs and to the repeated reheating related to the layer-wise fabrication principle of the LPBF process. Best et al. [28,48] achieved similar results, explaining the lower toughness by a high oxygen content, compared to lab-grade as-cast samples. Bordeenithikasem et al. [25] investigated the mechanical properties of a Zr-based BMG, with the trade name AMZ4, produced by LPBF. They performed bending, hardness, and wear tests and observed that crystallization caused brittleness and deteriorated the mechanical properties, such as flexural strength [25].

To use AM for industrial applications, dimensional accuracy is also important apart from the mechanical properties of the manufactured parts. To our best knowledge, there is up to now no literature on the dimensional accuracy of complex BMG parts produced via AM. Benchmarks are typically used to test the geometrical accuracy of LPBF processing and to evaluate the performance of printing machines for the fabrication of different shapes and sizes. Each feature targets specific purposes, e.g., cubes for evaluating flatness, linear accuracy, and parallelism of faces and edges [49–51]. Ilčík et al. [52] and Kruth et al. [53] investigated the accuracy of LPBF with crystalline alloys via benchmarks. The best-achieved accuracy was around 20 μm.

In this work, we characterized printed Zr-based BMG (AMZ4) samples and detected nanocrystals via synchrotron X-ray diffraction (XRD) and field-emission scanning electron microscopy (FESEM). The crystallization is explained from analysis of numerical finite element modeling (FEM) and fast differential scanning calorimetry (FDSC) investigations. We further analyzed the physical and mechanical properties of the samples, and found that despite the presence of nanocrystals in the amorphous structure, good mechanical properties with respect to compressive and flexural strength, nano- and microhardnesses, and wear resistance are achieved. We also printed a benchmark with complicated geometrical features and illustrated an excellent dimensional accuracy for these printed structures.

2. Materials and methods

In this study, Zr-based metallic glass powder (trade name AMZ4) with a nominal composition of $Zr_{59.3}Cu_{28.8}Al_{10.4}Nb_{1.5}$ (in at.%, supplied by Heraeus Additive Manufacturing GmbH) was used. The powder particle-size distribution ranged from 10 μm to 50 μm ($D_{10} = 16$ μm, $D_{50} = 30$ μm, and $D_{90} = 47$ μm).

LPBF sample manufacturing was undertaken using a TruPrint 1000 machine with a 200 W fiber laser (wavelength 1070 nm) and a spot size of 30 μm, using nitrogen as a protective gas. The printing parameters corresponding to the laser power, scanning speed, hatching distance, and layer thickness were 30 W, 600 mm/s, 90 μm, and 20 μm, respectively. Two different substrate materials, i.e. stainless steel and an Al alloy (Al-Mg-Si1), were used.

Conventional DSC measurements were performed with a Netzsch DSC 204 F1 Phoenix at a heating rate of 0.33 K/s (20 K/min). FDSC measurements of the AMZ4 powder were carried out with a Flash DSC 2+ (Mettler Toledo) equipped with UFH1 sensors. The AMZ4 alloy could not be fully melted during these measurements due to the limited maximum temperature of the sensors. Therefore, only heating experiments were performed to determine the crystallization temperature of the amorphous AMZ4 powder at high heating rates. The sample oxidation was minimized by applying 50 ml/min Ar gas flow during the measurements.

XRD characterization of the samples was done with a PanAlytical Empyrean diffractometer (Theta-Theta, 240 mm), equipped with a PIXcel-1D detector in reflection mode using CuKα radiation. Synchrotron XRD was carried out to detect the presence of nanocrystals in the amorphous matrix. The tests were performed at the MS beamline [54] of the Swiss Light Source, Paul Scherrer Institute (PSI), using a wavelength of 0.4915 Å in transmission mode and a Pilatus 6 M detector. The X-ray beam-spot size was 100 μm and three points were tested on a lamella of thickness 80 μm. The detector position was calibrated with a LaB_6 NIST SRM 660b standard using the software DIOPTAS [55] and the 2D images were integrated along the entire azimuthal range using the software described in [56]. Each point was exposed to the X-ray beam for 10 s.

Micro-Computed Tomography (μ-CT) analysis was carried out on a cylinder with 3 mm diameter and 3 mm height, using an EasyTom XL Ultra 230–160 micro/nano-CT scanner (RX Solutions, Chavanod, France). The scanner operated at 230 kV and 65 μA. An Al—Cu filter was interposed between the X-ray source and the samples. The samples were scanned over 360° with a rotation step of 0.25° and a frame average of 20. The nominal resolution was set to 2.0 μm voxel size. Scan images were reconstructed using a moderate beam-hardening correction.

The obtained tomographic cross-sections (16-bit TIFF format) were segmented with the application of a global threshold to quantify porosity as a percentage of the sample's bulk volume.

For the microstructural study, a sample was cut and ground with sandpapers (until grit 2500) and polished with a suspension of alumina particles until 1 μm size. The melt pool was revealed by etching with an acid solution (45 ml water +45 ml HNO_3 + 10 ml HF) at room temperature. Optical microscopy (OM, Leica DM6000M) and scanning electron microscopy (SEM, ZEISS GemniSEM450), equipped with energy-dispersive X-ray spectroscopy (EDS), were used for measuring the accuracy of different features in a benchmark and studying the microstructure in the melt pool and the HAZ.

Oxygen analysis was performed applying the carrier-gas hot-extraction method, using a LECO OHN 836 analyzer. The final values were obtained upon averaging of at least three measurements. The mass of each sample (powders and bulk-printed samples) was about 100 mg, and the device was calibrated before each set of measurements using Zr calibration samples provided by LECO.

The Young's modulus of the printed materials was measured by ultrasonic resonance frequency using a Grindosonic (Lemmens N.V., Belgium) device on a bar with size $50 \times 5 \times 4$ mm^3.

The compressive strength of the samples with a height of 9 mm and a diameter of 6 mm was determined from uniaxial compression testing using a Gleeble 3800 machine at a strain rate of 1×10^{-4} s^{-1}. Three-point bending tests were carried out on three samples ($40 \times 5 \times 3$ mm^3) with a support span of 30 mm, using a Schenck machine at a displacement rate of 830 nm/s.

Vickers microhardness tests were conducted with 1, 2, and 5 kgf (HV 1, 2, and 5, respectively) and a dwell time of 10 s with a Qness Q10A machine. Hardness mapping (10×10 μm^2 area, 1600 indents) on the polished (down to 1 μm) cross-section of the amorphous as-built sample was performed using a Nano Indenter® G200 (KLA company) at an indentation load of 1 mN with a cube corner indenter.

Sandblasting was performed on the as-built benchmark using a Master Problast 3 system (Vaniman Manufacturing Co.) with a particle size of 50–100 μm. The roughness of a benchmark LPBF part was measured with a VK-X1000 Series 3D laser scanning confocal microscope. The software provided by the manufacturer (MultiFileAnalyzer version 2.12.17) was used for processing the data and the roughness was measured based on ISO 25178-2 standard. Wear tests were performed with a home-made reciprocating tribometer [57] on a sample ground with sandpapers (until grit 2500). An Al_2O_3 ball was used as a counterpart to rub on a fixed LPBF-processed Zr-based BMG sample. The force and speed were 2 N and 6 mm/s, respectively. Three wear tracks were tested and each test was carried out for 30 min with a frequency of 1 Hz. The total reciprocating distance was 10.8 m for each test. Afterward, the sample was put in an ultrasonic bath to remove the debris and wear products as much as possible. Then, the average of the volume loss was measured using the confocal microscope.

3. Results and discussion

3.1. Characterization

Fig. 1 shows an XRD pattern of the gas-atomized powder. It reveals two broad halo peaks, which illustrate that the powder is amorphous. The spherical shape of the powder particles indicates that the powder flowability is likely suitable for LPBF processing. The oxygen content of the powder was 1300 ± 16 ppm, which is much higher than that of a lab-grade as-cast sample, which was reported as 168 ± 61 ppm [28].

Fig. 2a shows printed cuboids and cylinders, where the latter were used for compression tests. Fig. 2b illustrates that the samples underwent stress-induced distortion (5 mm thick +1 mm support), but without crack initiation. Apart from the presence of residual stresses, the reason for the detachment of the sample from the substrate may be due to its higher melting point compared to AMZ4. The power used in the LPBF process may thus not be high enough to generate a strong bonding between the sample and the substrate in the sample corners. This effect is expected to be more pronounced when a larger sample is printed due to higher levels of residual stress. Thus, in a further experiment, an Al alloy was used as a substrate and better bonding was obtained, as can be seen in Fig. 2c and d. All further analyses in this work were done on the samples fabricated on Al-alloy substrates. The oxygen content of the manufactured part was 1480 ± 9 ppm. This infers that during production, the oxygen content was increased by almost 200 ppm.

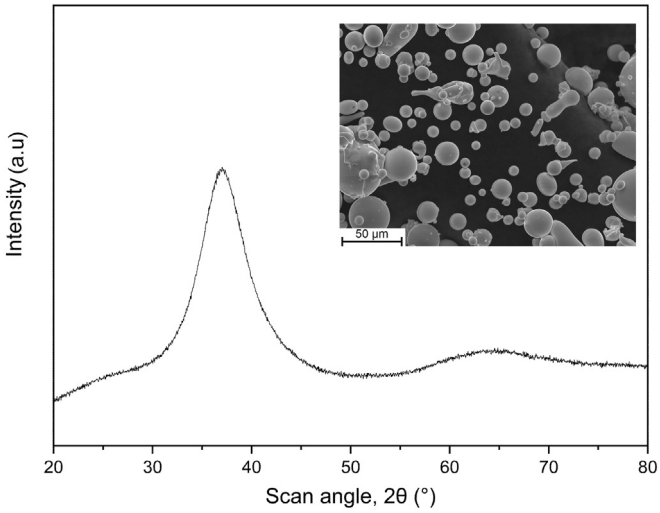

Fig. 1. Laboratory XRD pattern (CuKα radiation) of the gas-atomized powder. The inset shows an SEM image of the powder particles, which mostly have a spherical shape.

A cylinder with a diameter and height of 3 mm was produced for μ-CT analysis. Fig. 3a shows the 3D distribution of defects inside the sample. The volumetric density of the sample was measured as 99.82% and no cracks were detected. To the authors' knowledge, this is the highest reported density for AMZ4 alloys prepared by AM. A histogram of the defects' size distribution is presented in Fig. 3b. The majority of the defects (86%) had a size between 0 and 5 μm, and no defects larger than 35 μm were found. Fig. 3c–d shows two snapshots of X-Y and X-Z cross-sections, respectively. The defects are shown in black color inside the sample. Most of them represent porosities, according to their circular cross-section.

Fig. 4a shows a laboratory XRD pattern of a printed sample. It indicates a globally amorphous structure with a small amount of crystalline phase, as visible from the little shoulder marked by a red arrow. Further investigation was done by synchrotron XRD experiments to detect the potential presence of nanocrystals. Fig. 4b presents the diffraction of three randomly chosen areas (not shown here) of the sample. The different diffraction angles, 2θ (Fig. 4b–c), compared to the laboratory method (Fig. 4a) are due to the different X-ray wavelengths deployed, i.e. 0.4915 Å in the synchrotron experiments compared to 1.5418 Å obtained from the CuKα X-ray source. For two of the point measurements (P2 and P3) tiny peaks are detectable, which correspond to the presence of nanocrystals. Fig. 4c shows the diffraction pattern of P2 for longer time exposure (60 s). Several peaks are clearly visible and have been identified to correspond to the Cu_2Zr_4O phase, which appears to crystallize early during the crystallization process [58,59]. This phase is a $NiTi_2$-type phase [60] with space group $fd\bar{3}m$ and with a unit cell of 11.953–12.088 Å [39,59,60]. Fig. 4d and e show SEM images of the X-Z cross-section after etching for 20 s. The average width (measured in 30 locations) of the HAZ is 2.13 ± 1 μm and nanocrystals are distributed in the amorphous matrix. The area fraction of crystals in the single track in Fig. 4d is 4.5%, as analyzed by ImageJ® software. After applying a threshold, the micrograph was turned into a black-and-white image

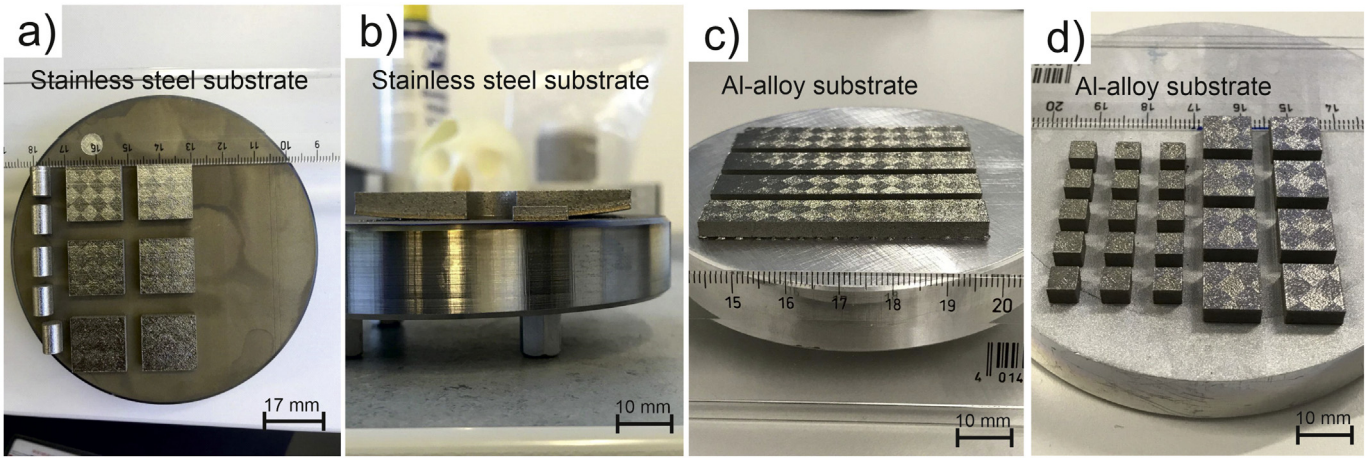

Fig. 2. (a) Printed cuboids with an area of $17 \times 17\ mm^2$ and heights of 1, 2, and 3 mm, plus horizontal cylinders with a diameter of 6 mm and a height of 9 mm, on a stainless steel substrate. (b) Residual stress-induced sample distortion on a stainless steel substrate. (c) Printed cuboids with a size of $60 \times 10 \times 4\ mm^3$ on an Al-alloy substrate. (d) Printed cuboids with an area of $10 \times 10\ mm^2$ *and* $5 \times 5\ mm^2$ and a height of 4 mm on an Al-alloy substrate.

and the fraction of black pixels (corresponding to nanocrystals) was measured in the area of interest. It is thus confirmed that the shoulder in Fig. 4a and the small peaks in Fig. 4b are due to nanocrystals, in agreement with the results of Pacheco et al. [38].

Fig. 5 reveals FDSC traces of the AMZ4 powder at a high heating rate of 10,000 K/s. Ericsson et al. [61] used FDSC to plot a TTT diagram of AMZ4 during cooling and mentioned that the critical cooling rate of the alloy is lower than 20,000 K/s. In that work, however, only the time for reaching the crystallization peak was reported, so that the percentage of crystallization could not be extracted. In AM, the heating in the HAZ determines the crystallization, whereas the cooling from the melt is generally fast enough to avoid crystallization. In fact, based on the simulation results presented later, the cooling rate in the melt pool is around 5×10^5 K/s. Thus, it is important to investigate the behavior of the material during heating. In FDSC, it is possible to detect the onsets of glass transition and crystallization even at very high heating rates. Crystallization, however, could not be prevented for the AMZ4 powder even at the maximum heating rate of the FDSC device, which is 50,000 K/s.

The inset of Fig. 5 shows conventional DSC results of the powder and the LPBF sample at a heating rate of 0.33 K/s. Up to now, the glass

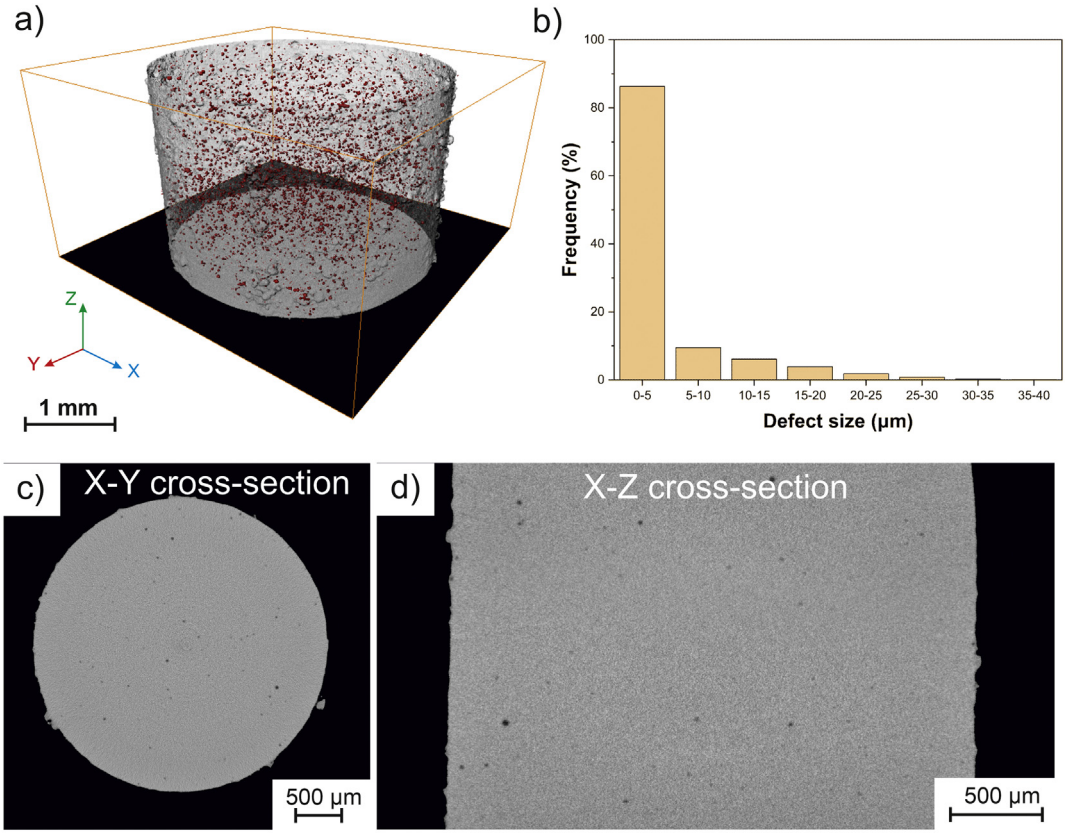

Fig. 3. μ-CT analysis of a cylinder with 3 mm diameter and height. (a) 3D distribution of defects inside the cylinder, (b) histogram of the defects' size distribution, (c) snapshot of X-Y cross-section (defects are shown in black), and (d) snapshot of X-Z cross-section.

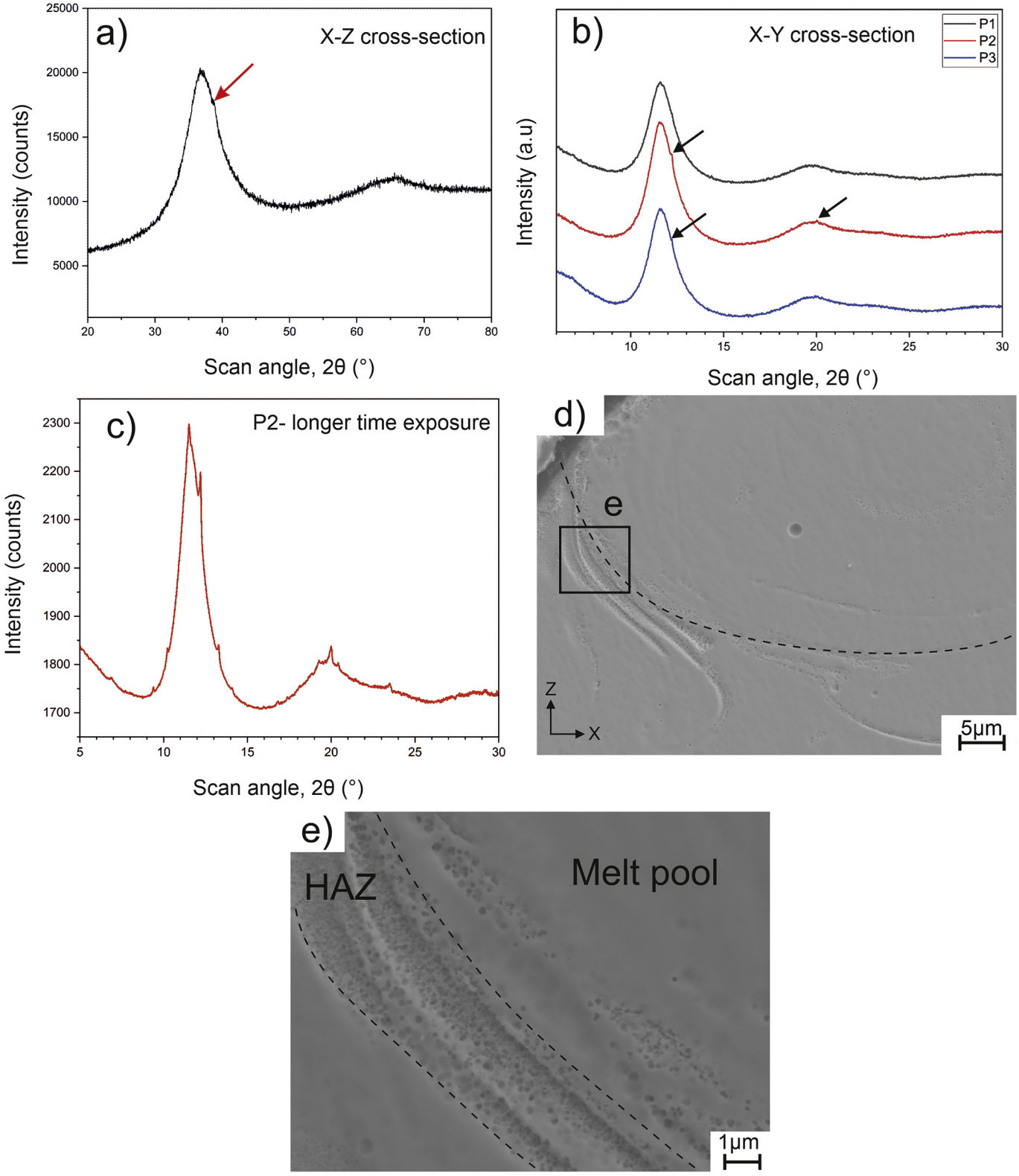

Fig. 4. (a) Laboratory XRD pattern (using CuKα radiation) of the printed sample, ground with sandpapers until grit 2500. (b) Synchrotron XRD patterns of three randomly chosen points (P1-P3) of the X-Y cross-section (c) Synchrotron XRD pattern of P2 after longer time exposure (60 s). (d) SEM secondary electron image of the X-Z cross-section, indicating the presence of an HAZ. (e) Higher-magnification image of the area marked by a rectangle in (d), clearly revealing nanocrystals in the HAZ.

transition and crystallization temperatures were measured at a low heating rate (often 0.33 K/s) [15,16,36,35,62–66] to explain crystallization in the AM of BMGs. Our FDSC results show, however, that the glass transition and crystallization temperature shift to significantly higher temperatures due to the higher heating rate applied (see Table 1). As the onset temperature of crystallization measured at higher heating

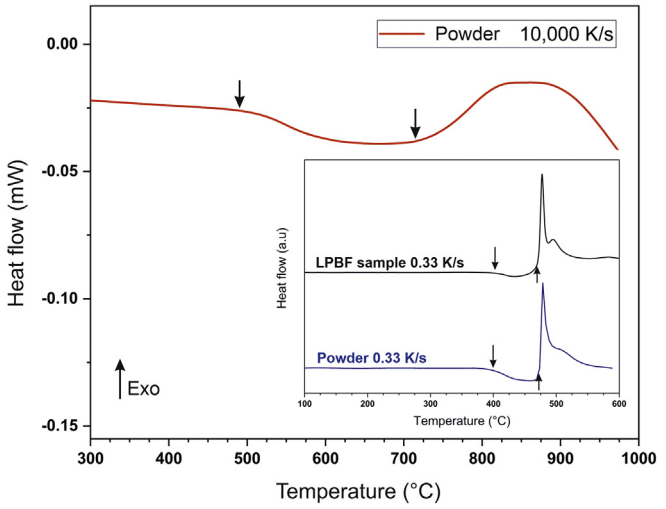

Fig. 5. FDSC scan of AMZ4 powder measured at a heating rate of 10,000 K/s. The inset shows conventional DSC results of the powder and LPBF sample measured at a heating rate of 0.33 K/s (20 K/min). The arrows indicate the onsets of glass transition and crystallization (see also Table 1).

Table 1
Onset of glass transition and crystallization temperature, and enthalpy of crystallization, extracted from conventional DSC and FDSC tests of the powder and LPBF samples shown in Fig. 5.

Sample	Heating rate, K/s	T_g^{onset}, °C	T_x^{onset}, °C	ΔH, J/g
Powder	10,000	483	702	N/A
Powder	0.33	402	471	−82.1
LPBF	0.33	404	471	−77.6

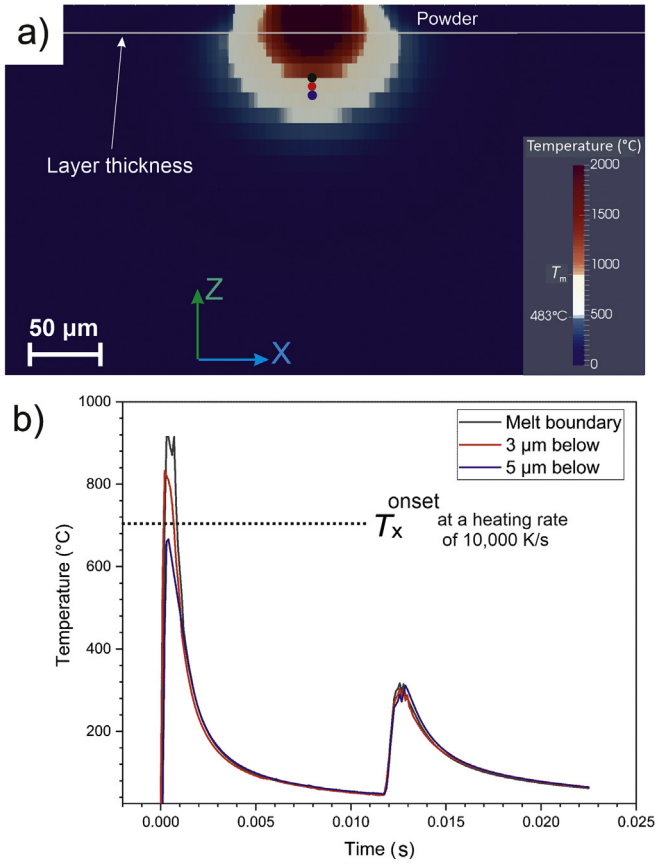

Fig. 6. a) Simulated temperature distribution of a laser track with a power of 30 W, scanning speed of 600 mm/s, hatching distance of 90 µm, and layer thickness of 20 µm in X-Z cross-section. b) Thermal history of three points, illustrated in (a), where one is located at the melt-pool boundary and the others 3 and 5 µm below it.

rate is closer to the heating rate used in laser processing, it should be used as a reference crystallization temperature for the AM process in the future.

To better understand the reasons for crystallization, we performed numerical simulations of the LPBF process with a dedicated in-house finite element (FEM) code (see Refs. [67, 68] for more details). A two-laser tracks FE simulation was run based on the thermal and physical properties given in Table A1–A3 (see Appendices). Fig. 6a shows the simulated temperature distribution (in X-Z cross-section) for the sample fabricated with a power of 30 W, scanning speed of 600 mm/s, hatching distance of 90 µm, and layer thickness of 20 µm. The depth of the melt pool is 55 µm, which is in good agreement with the experimental value of 58 ± 5 µm. Fig. 6b presents the thermal history of three points, where one is located at the melt-pool boundary and the others 3 and 5 µm below it. Comparing these three points reveals a high temperature gradient in the HAZ, which is helpful for reducing its size. Yang et al. [36] studied the effect of complex shapes on the crystallization of LPBF-processed samples. They stated that the time for crystallization at a temperature close to the melting temperature is very short and it is challenging to suppress crystallization. For the point that is located 5 µm below the melt pool, the peak temperature is 666 °C, which is lower than the onset temperature of crystallization at a heating rate of 10,000 K/s, i.e. 702 °C (see Table 1). Based on the simulation, the calculated heating rate is approximately 10^6 K/s. As a higher heating rate shifts the glass transition and crystallization temperatures to higher values (e.g. [47]), we expect no crystallization at the location 5 µm below the melt-pool boundary, but for the point located 3 µm below it crystallization is anticipated. In fact, the simulations are in good agreement with the experimental results (Fig. 4d and e), which show that nanocrystals are dispersed along the HAZ on on length scales below 5 µm.

3.2. Mechanical properties

Table 2 compares the microhardness (HV 1, 2, and 5) of our study with results from the literature. Although we detect nanocrystals by laboratory XRD, synchrotron XRD and SEM, we obtain lower or equal hardness compared to those in literature, where fully or XRD amorphous structures have been reported. Refs. [39, 40] reveal that (nano-)crystallization should lead to an increase in hardness for AMZ4, which may be a hint that the X-ray amorphous samples of the literature also contain some nanocrystals. Shen et al. [69] mentioned that laboratory XRD and conventional DSC are not the best methods to detect a few percentages of crystallization.

Fig. 7a is a schematic image illustrating that the nanoindentation tests were carried out almost in the middle of the X-Z cross-section of the sample. An SEM micrograph of the tested region is presented in Fig. 7b. A nanohardness map (Fig. 7c) shows that the sample is relatively homogenous. The average value after 1600 indentations is 5.13 ± 0.25 GPa. Marattukalam et al. [39] reported a higher nanohardness for an LPBF processed sample, which was XRD amorphous and had less than 0.7% crystallization based on DSC results. Fig. 7d presents the corresponding histogram, which is close to a Gaussian distribution, and thus consistent with a low volume fraction of nanocrystals in the tested area. The presence of nanocrystals may be correlated with the red spots in Fig. 7c.

Table 2
Hardness (HV1, 2, and 5) of as-cast and LPBF processed samples.

Sample	Condition	State	Characterization method	Hardness (HV 1)	Hardness (HV 2)	Hardness (HV 5)
AMZ4 [25]	As-cast	Amorphous*	XRD, DSC	–	455	–
AMZ4 [70]	As-cast	Amorphous*	XRD	–	–	466.9
AMZ4 [28]	As-cast	Amorphous*	XRD, DSC	469 ± 2	–	–
AMZ4 [28]	LPBF	Amorphous*	XRD, DSC	466 ± 4	–	–
AMZ4 [32]	LPBF	Amorphous*	XRD	–	–	484 ± 7
AMZ4	LPBF	Highly amorphous	Conventional and synchrotron XRD, DSC, FDSC, SEM	465 ± 5	455 ± 8	446 ± 9

* Reported by the authors.

The Young's modulus of the highly amorphous sample was measured by ultrasonic resonance frequency as 83.3 GPa (three measurements performed on a specimen). Although nanocrystals are present, this value is similar to that reported for the same material in Ref. [25].

The flexural strength of the Zr-based BMG was investigated using a three-point bending test. From the expression relevant to rectangular bars [71],

$$\sigma_f = {}^{3FL}/_{2bd^2}, \quad (1)$$

where F is the applied force (load), L the length of the support span, b the width of the test sample, and d its thickness, a value of 1666 ± 33 MPa was obtained. This value is among the best results achieved in bending for BMGs produced by additive manufacturing methods. No plastic deformation on the macroscale was detected during the test (see Fig. 8a). Compared with the four-point bending test of Bordeenithikasem et al. [25] performed on an alloy of the same composition (AMZ4) and hardness, and processed in a similar way, the strength measured in our study is about 12% higher. This may be due to the presence of a higher porosity content of the sample in Ref. [25] (99.4% density, determined by the Archimedes method) compared to a density of 99.82% achieved in the current study (determined via micro CT). Bordeenithikasem et al. [25] showed that lack of fusion (LoF) is present in the printed part. LoF often results in sharp corners and the stress intensity at those regions can locally increase and act as a critical notch to cause early failure [72]. Bochtler et al. [70] investigated the thermoplastic forming of AMZ4 powder. Via a three-point bending test, they achieved a flexural strength of 650 MPa, which is far lower than what is obtained in the current study. The reason for such a low flexural strength is due the powder particles that did not fuse but were just poorly connected.

As outlined for example in Refs. [73, 74], plastic strain in metallic glasses is localized into shear bands of nanoscale thickness at temperatures below $\approx 0.8T_g$. Fig. 8b and c show the fracture surface of one of the samples after failure. Several shear bands can be seen on the sample side close to the crack (see blue arrows in Fig. 8c). As soon as the shear bands initiate, they propagate rapidly in a stick-slip motion [75], and thus the fracture of BMGs generally occurs along one dominant shear band. This mechanism results in a low ductility at the macroscopic level (Fig. 8a).

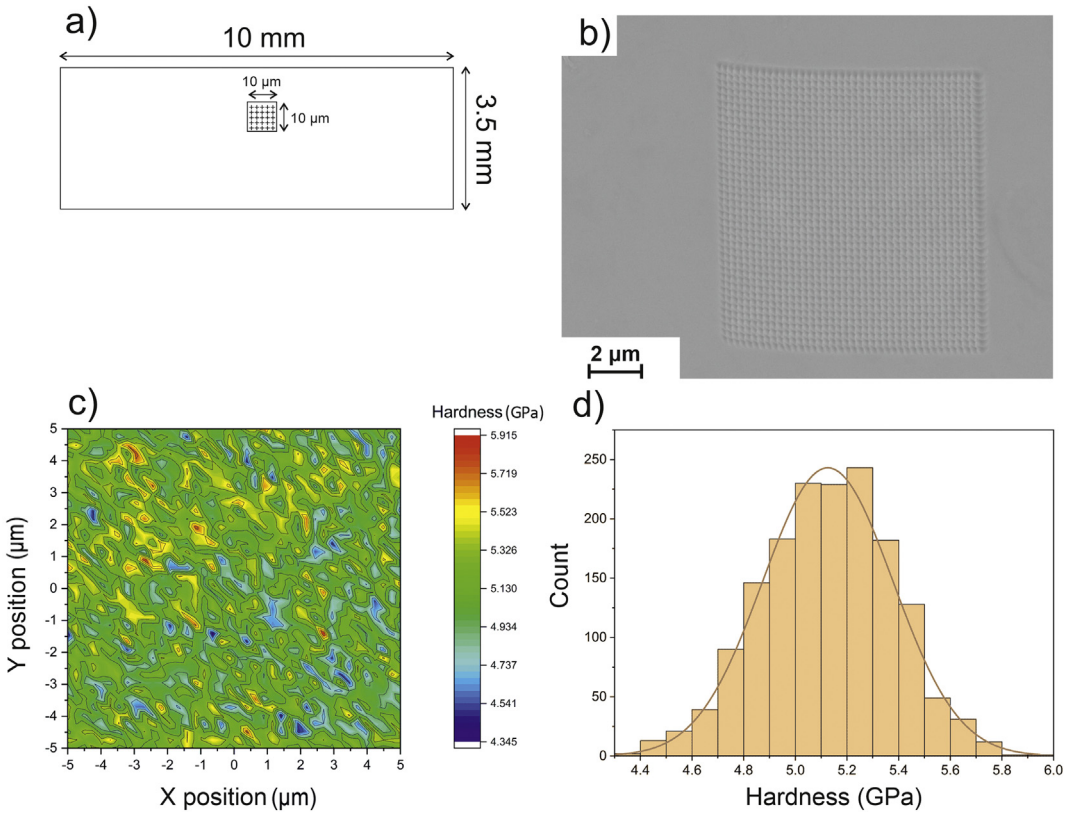

Fig. 7. (a) Schematic view revealing the position of the nanoindentation tests in the sample. (b) SEM micrograph of the 1600 indents performed. (c) Nanohardness map of the $10 \times 10\,\mu m^2$ area tested. (d) Histogram revealing a Gaussian distribution in hardness.

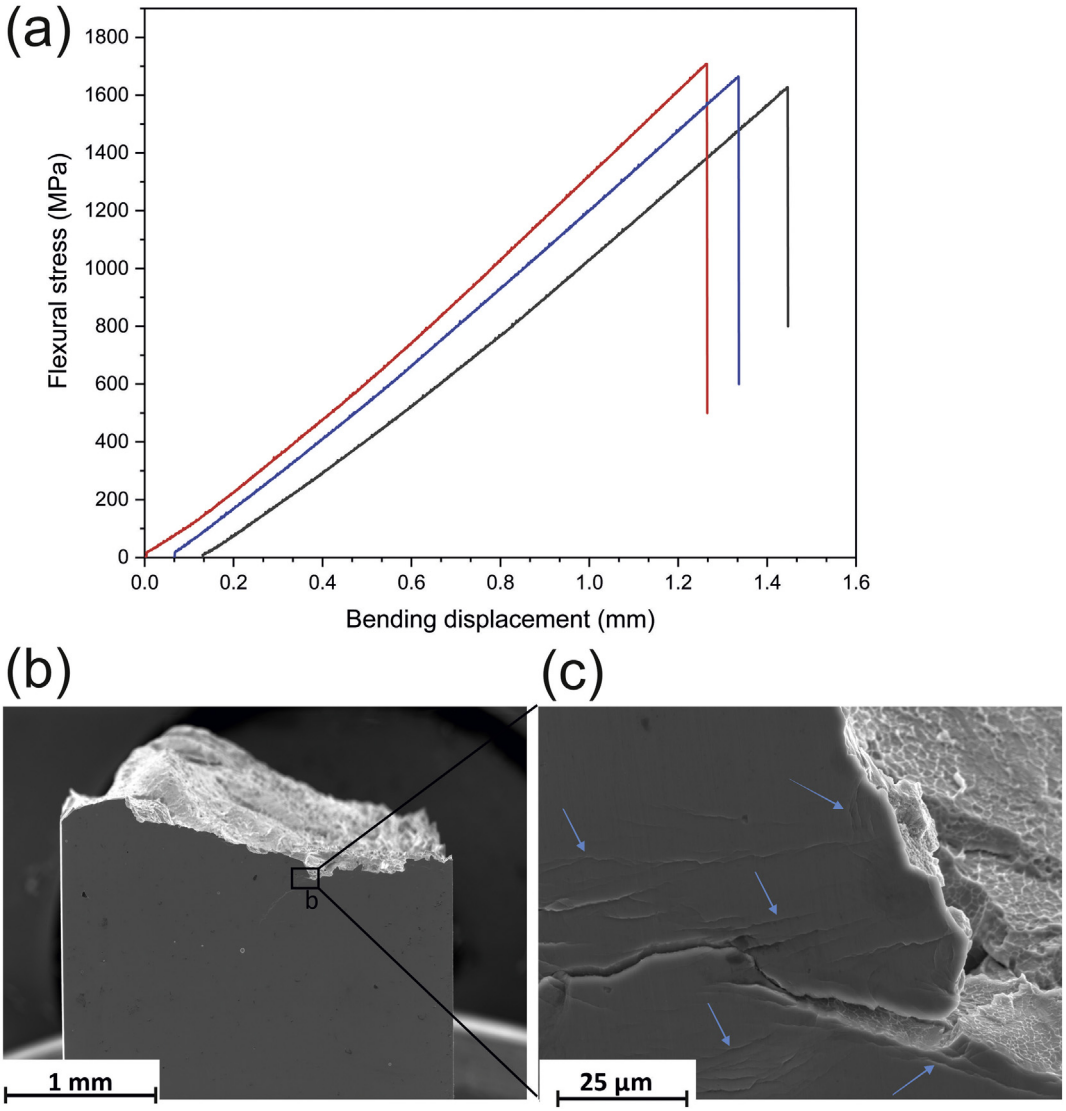

Fig. 8. (a) Stress-displacement curves from three-point bending tests. (b) Macroscopic side-view image of a sample after failure. (c) Higher-magnification image of the area marked in (b), showing shear bands (marked by blue arrows).

The compressive yield strength of the cylinders was measured as 1368 ± 41 MPa (not shown) and the strain to failure was 1.64 ± 0.05%, again without any detection of plastic deformation at the macroscopic scale. To our knowledge, there are no other results reported on the (macroscopic) compressive properties of AMZ4 fabricated via AM methods. The mentioned values are lower than those reported by Best et al. [28] for LPBF-processed AMZ4 (1.82 GPa). These authors performed compression tests with a nanoindentation system at a deformation rate that was about 40 times lower than in the current study. Furthermore, they investigated micropillars of 2 µm diameter and 5 µm height, where a size effect for such small geometry is expected. Effects of nanocrystals and defects, such as porosity and/or LoF, were not taken into account. In Ref. [48], the compressive yield strength of the as-cast sample was measured and found to be 1.7 GPa, but the test condition and sample size were not reported. Because of the presence of defects in the LPBF-processed samples, they generally show a lower compressive strength than the as-cast alloys; see Refs. [33, 35, 41].

The fracture surface after the compression test is presented in Fig. 9. The fracture angle is around 45° with respect to the compression direction (Fig. 9a) and vein-like patterns (indicated by arrows) are visible in Fig. 9b. The latter can be found in many areas of the fracture surface. Two areas in Fig. 9b are enlarged in Fig. 9c and d. These patterns are attributed to significant softening or reduced viscosity during fracture [76]. In the final stage of the fracture, the temperature significantly increases because of the instantaneous release of stored elastic energy. Fig. 9d shows liquid-like features and droplets (marked by arrows), illustrating localized temperature increase on the fracture surface, as suggested by Bruck et al. [77] and Liu et al. [78].

Wear experiments were performed to study the wear resistance and tribological behavior of LPBF-processed AMZ4. The wear rate, W, is defined as the ratio between the volume loss due to wearing and the total reciprocating distance (in units of $mm^3\ m^{-1}$, or $10^{-9}\ m^2$). The measured value for our Zr-based BMG is 2.4 (± 0.8) $\times\ 10^{-4}\ mm^3\ m^{-1}$. A dimensionless value is obtained when dividing the wear rate by the contact area, A_n, but this dimensionless value changes with the applied pressure at the contact point. The effect of the normal force, F_n, was therefore introduced, which defines the wear-rate constant (in MPa^{-1}) [79],

$$k_a = {}^{W}/_{F_n}, \tag{2}$$

reflecting the tendency of the material to wear.

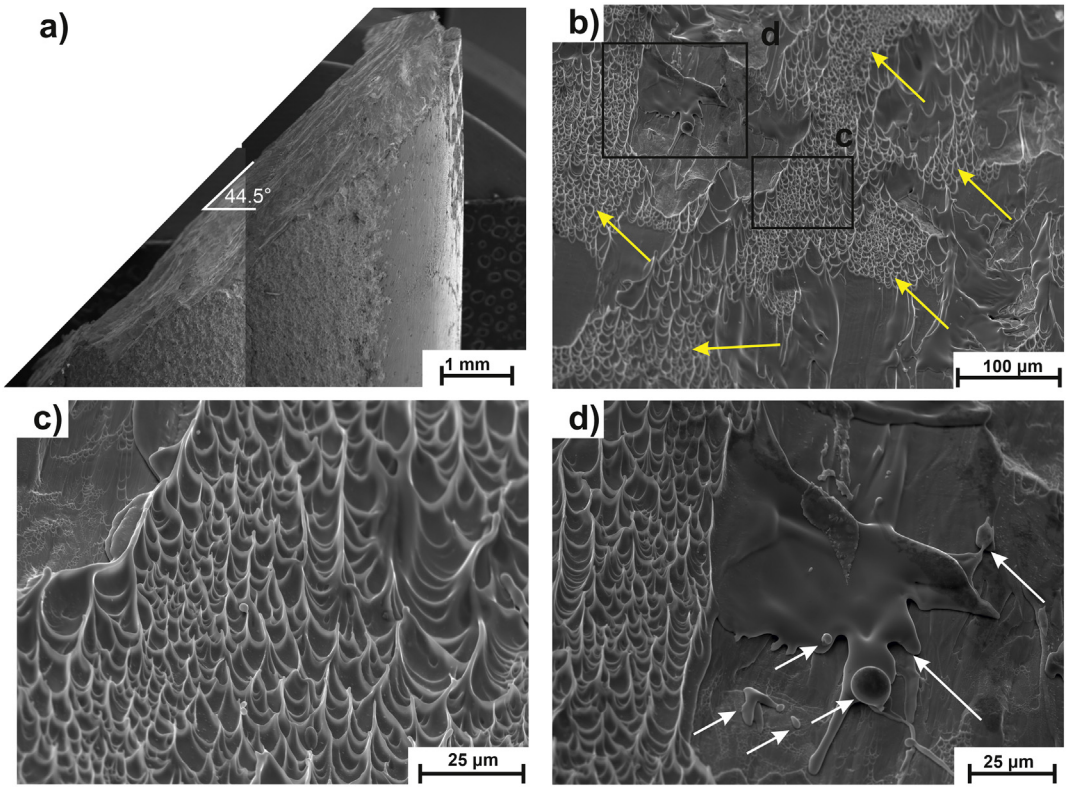

Fig. 9. Fracture surface after compression test. (a) The fracture angle is inclined by around 45° with respect to the compression direction, which is typical for BMGs. (b) Vein-like patterns on the fracture surface, indicating significant softening upon fracture. (c) Higher-magnification image of the area c in (b), detailing a vein-like pattern, and (d) higher-magnification image of the area d in (b), showing droplets (as marked by arrows).

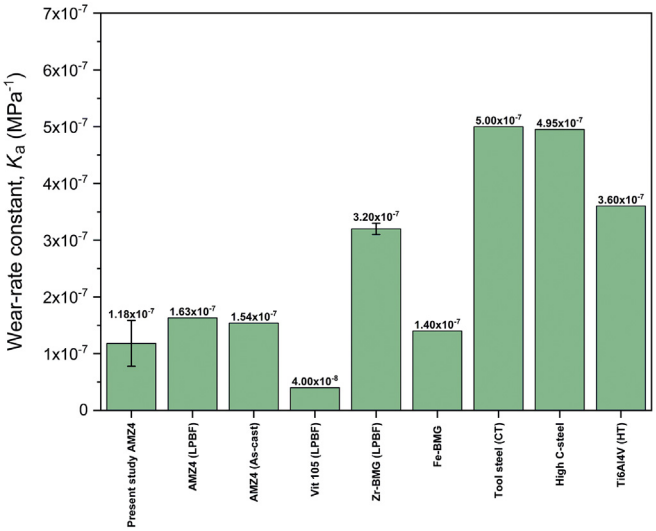

Fig. 10. Comparison of wear-rate constants among our AMZ4 processed by LPBF; AMZ4 processed by LPBF and as-cast [25]; Vit 105 ($Zr_{52.5}Cu_{17.9}Ni_{14.6}Al_{10}Ti_5$) processed by LPBF [29]; a Zr-based BMG ($Zr_{60.14}Cu_{22.31}Fe_{4.85}Al_{9.7}Ag_3$) processed by LPBF [27]; an Fe-based BMG used as coating and produced by laser cladding [80,81]; a cryogenically treated tool steel produced conventionally [82]; a high-carbon steel produced conventionally [83]; and heat-treated Ti6Al4V produced conventionally.

Fig. 10 shows a comparison of the wear-rate constants among the Zr-based BMG we produced and several other functional alloys. Apart from Vit105 produced by LPBF, the average value of the Zr-based BMG (AMZ4) of the present study is better than that of all other reported values, including those of BMGs. The average value of the wear-rate constant of AMZ4 obtained in our study is also lower than that measured by Bordeenithikasem et al. [25], although the hardness of these samples is almost similar. Again, this may be due to the presence of a higher porosity content (99.4% density) in Ref. [25] compared to a density of 99.82% in the current study. In general, the results illustrate that LPBF-processed Zr-based BMG (AMZ4) can be advantageously used in applications where high wear resistance is required.

Fig. 11 presents SEM images and an oxygen EDS map of one of the wear tracks. The wear products are mostly detected in the periphery of the wear tracks (see Fig. 11a–b). Fig. 11c presents an EDS mapping of the oxygen content for the area shown in Fig. 11b, revealing that the wear products are enriched in oxygen. These results are consistent with those of Zhang et al. [27], who identified the concurrent occurrence of abrasive-wear and oxidation-wear mechanisms.

3.3. Complex geometry and geometrical accuracy

Fig. 12 shows a CAD file and printed part of the selected benchmark, designed to challenge the fabrication of complicated geometries.

One of the advantages of the LPBF process over conventional methods is that the resulting product is near-net-shape. Table 3 lists the nominal sizes of the eight different features identified in Fig. 12a. The accuracy of the printed parts is assessed through the difference between measured and nominal characteristic lengths, performed nine times for each feature (Fig. 13). In the as-built condition, some powder particles remained attached to the printed part due to sintering (see Fig. 14a and Fig. 14b), which decreases the dimensional accuracy. The results extracted from optical microscopy (OM) and SEM are in that case similar (see Fig. 14a and 14c). However, after sandblasting, the improved accuracy due to the removal of the sintered particles (see Fig. 14d) is best revealed by SEM. In such a case, all eight investigated features have a size difference with the CAD geometry of less

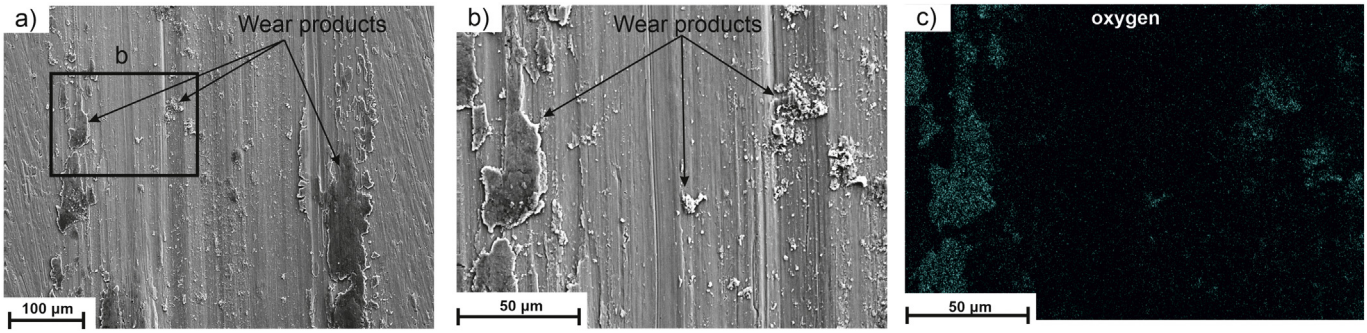

Fig. 11. (a) SEM image of one of the wear tracks, where wear products are clearly visible. (b) Higher-magnification image of region b marked in (a), and (c) EDS map of the oxygen content in (b).

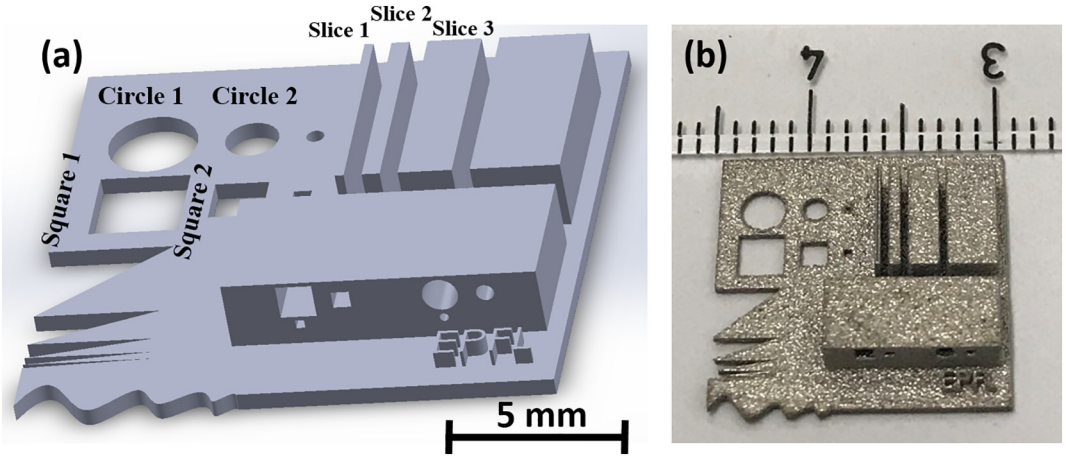

Fig. 12. (a) CAD file of a benchmark with complicated features, and (b) the benchmark fabricated from the Zr-based BMG via LPBF.

Table 3
Nominal characteristic dimensions of the eight different features in the benchmark shown in Fig. 12.

	Circle 1 (diameter)	Circle 2 (diameter)	Square 1 (side)	Square 2 (side)	EPFL (width of each letter)	Slice 1 (width)	Slice 2 (width)	Slice 3 (width)
Nominal size (μm)	2500	1500	2500	1500	105	250	500	1500

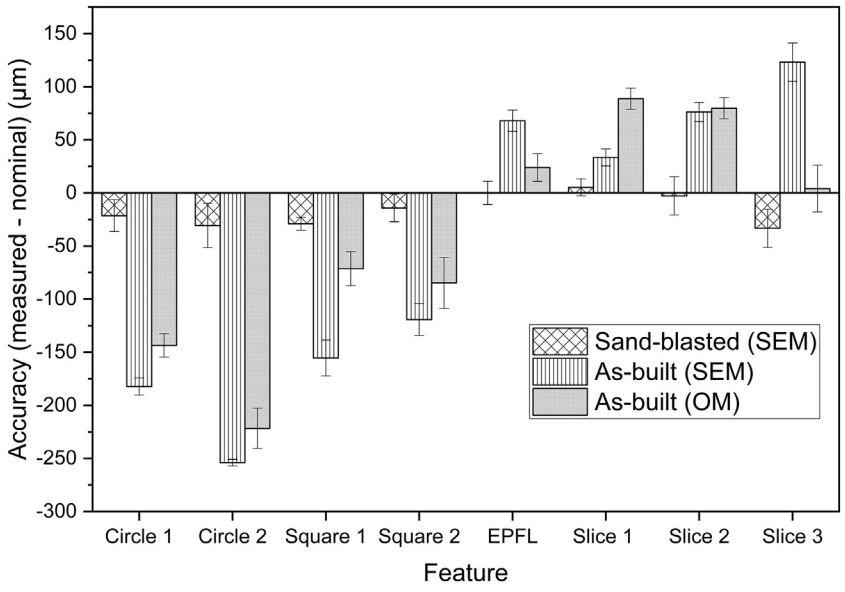

Fig. 13. Accuracy of the eight different features in the benchmark.

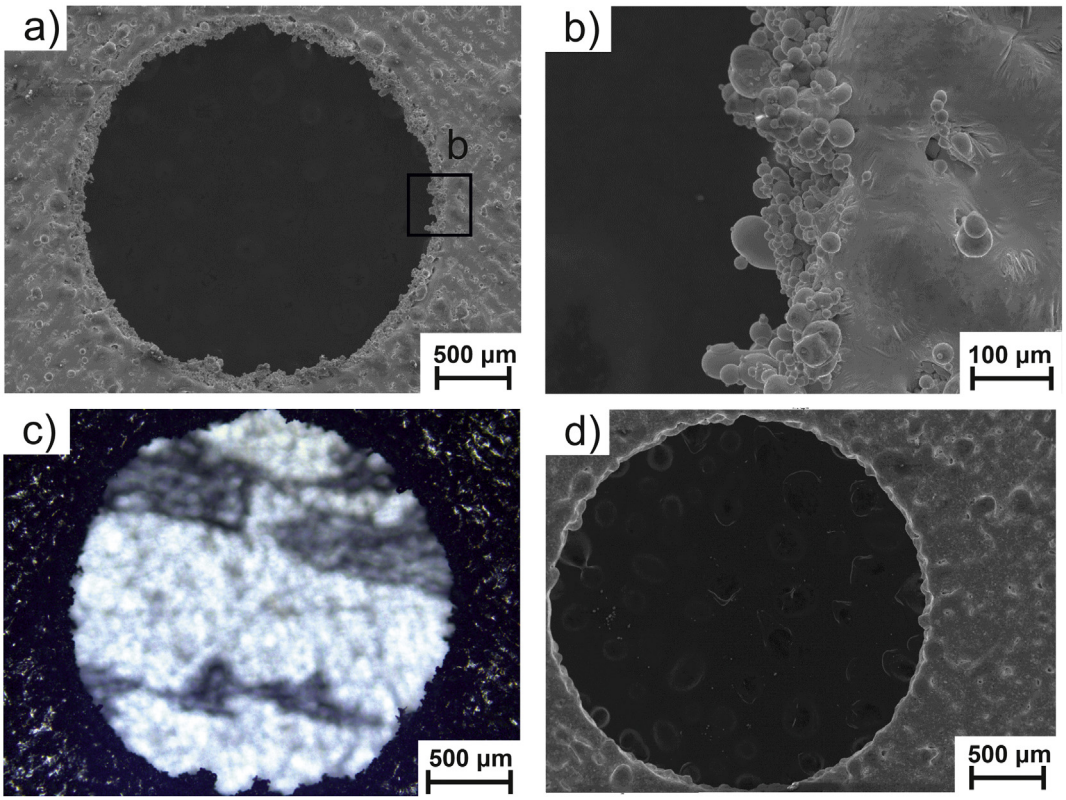

Fig. 14. (a) SEM image of Circle 1 in the as-built condition. (b) Powder particles sintered to the melted part (region b in (a) with higher magnification). (c) OM image of Circle 1 in the as-built condition, and (d) SEM image of Circle 1 with powder particles removed via sandblasting.

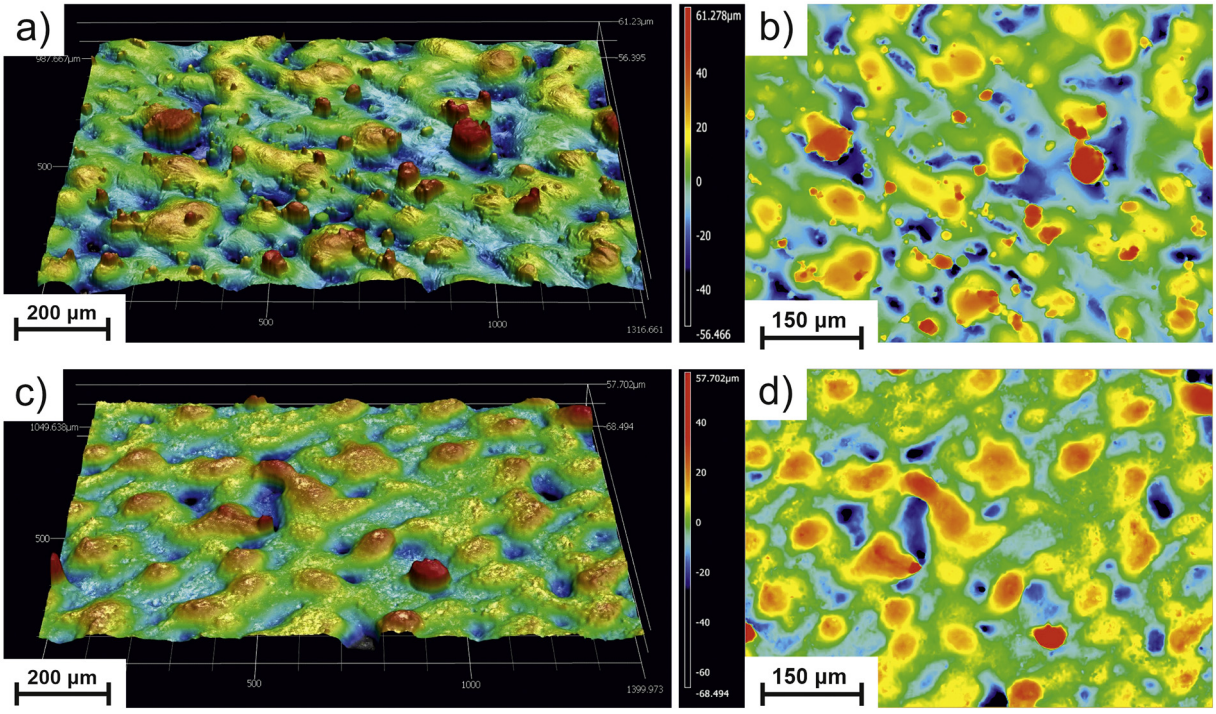

Fig. 15. Confocal microscopy of the benchmark shown in Fig. 12. (a) 3D image of the as-built condition, (b) top view of the as-built condition, (c) 3D image after sandblasting, and (d) top view after sandblasting.

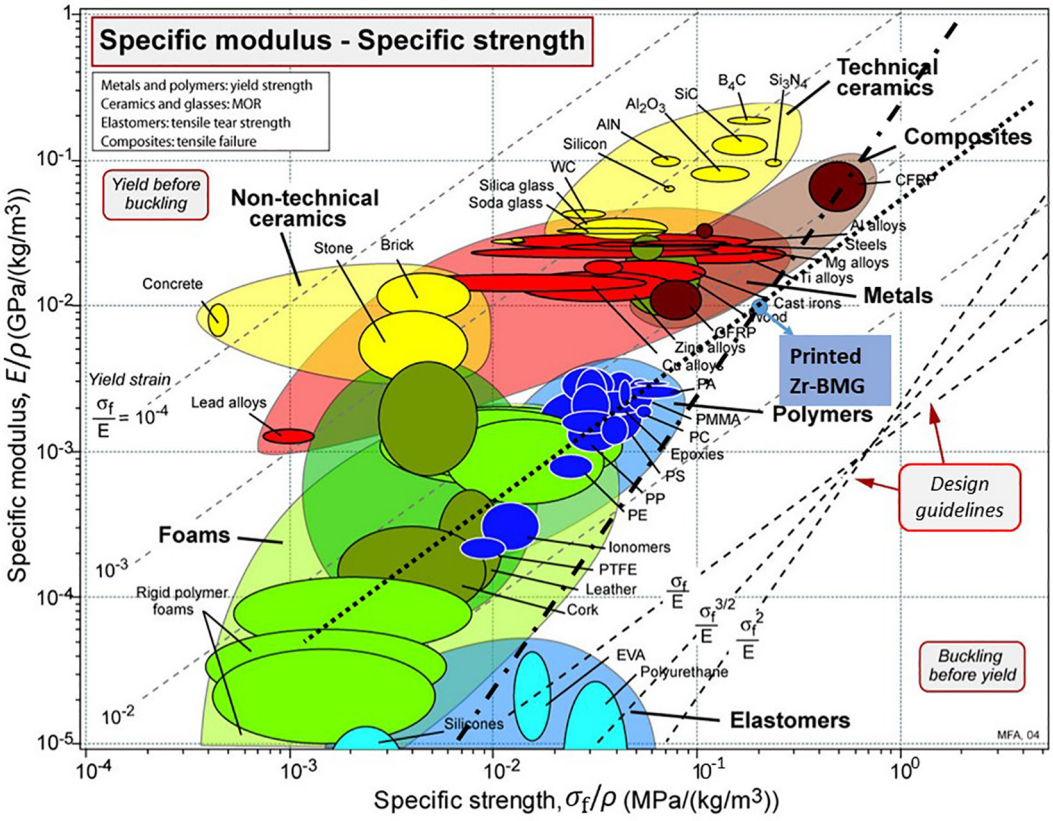

Fig. 16. Position of the LPBF printed Zr-based BMG in the diagram of specific modulus versus specific strength (modified from [79]).

than 40 μm, i.e., very close to the mean particle size (D_{50} = 30 μm, see section 2).

One reason for this high accuracy is the low amount of shrinkage during the solidification of BMGs compared to crystalline materials [84]. Using a thin layer thickness [85] and a small laser spot size also contributes to this impressive accuracy.

Low surface roughness of AM parts is essential for minimizing surface treatment after processing, especially when fatigue life and durability are of concern (e.g., for aerospace components [86] and medical devices [8]). Fig. 15a shows a 3D topography of the benchmark top surface in the as-built condition. In the presence of powder attached to the surface, the surface roughness, S_a, was 10.73 ± 0.77 μm. Fig. 15b presents the top view of the 3D image. The small red areas, revealing higher height, correspond to the attached (sintered) powder. The 3D image and top view of the surface after sandblasting are presented in Fig. 15c and d, respectively. In comparison with the as-built condition, the surface is more uniform. The surface roughness (S_a) of the sandblasted samples was measured as 6.95 ± 0.22 μm, which means that sandblasting is an effective method to remove powder particles and significantly decrease S_a.

3.4. A global outlook on LPBF fabrication of BMGs

Although LPBF has its own challenges in working with metallic glass powders, we have shown that LPBF can overcome size limitation, which is the main limiting issue for producing BMGs via conventional manufacturing methods.

The benchmark was successfully manufactured with high resolution and deviations of less than 40 μm were obtained. Zr-based BMGs have applications in sporting goods, diaphragms for pressure sensors, computers, smartphones, etc. They may be used in intricate gears mechanisms and micro-geared motors because of their high durability and excellent wear resistance, or as coil-shape springs because of their high elastic strain [8]. Zr-based BMGs may also be used in the jewelry field because of their superior scratch resistance and mechanical properties. Furthermore, except for roughness reduction in AM processes, there is usually no need for post-processing steps, e.g., those involving coating or oxide formation on the surface.

Considering the Young's modulus, density and yield strength of Zr-based BMGs produced by LPBF, one may consider the Ashby diagram of specific modulus vs. specific strength (see Fig. 16). This diagram has several design guidelines for different applications. For instance, σ_f^2/E is related to the design of lightweight springs and discs with maximum rotational velocity [79]. The LPBF-processed Zr-based BMG shows properties superior to crystalline metals, and equivalent to those of carbon-fiber reinforced polymer (CFRP) composites. On the other hand, σ_f/E is used in applications for which elastic deflection is more relevant [79]. In such a case, the LPBF-processed Zr-based BMG is superior to both crystalline metals and CFRP composites.

4. Summary and conclusions

In this study, we characterized in detail a Zr-based BMG alloy (AMZ4) manufactured via Laser Powder-Bed Fusion (LPBF), focusing in particular on its microstructure and mechanical properties. With respect to the latter, we quantified the alloy's micro- and nanohardness, compressive and flexural strength, and wear resistance. The outcome can be summarized as follows:

1) FDSC experiments show that the onset temperatures of glass transition and crystallization significantly shift to higher temperatures with an increase in heating rate. These increased temperatures are closer to the thermal conditions of the LPBF process and can thus be used to explain the crystallization of LPBF-processed BMGs.

2) Nanocrystals were detected in the heat-affected zones (HAZs) close to the melt-pool boundary. This is explained via a FEM model, which shows that the incubation time at temperatures close to the melting point is very short, but that cooling is not fast enough to avoid any crystallization.
3) Despite the presence of nanocrystals in the Zr-based BMG, excellent mechanical properties such as high hardness, wear resistance, and compressive and flexural strength were achieved in a sample with a density of 99.82% measured by micro-computed tomography.
4) Meticulous characterization via synchrotron experiments and electron microscopy is required to observe the nanocrystals, which may not be detectable via laboratory XRD. Advanced characterization tools are necessary to avoid conflicting results on the correlation between microstructure and mechanical properties of LPBF-processed BMGs.
5) A benchmark was printed and showed excellent geometrical accuracy with deviations of only 5–40 μm after sandblasting.
6) Potential applications include sporting goods or medical devices, for which properties are competitive with those of crystalline metals and carbon-fiber reinforced polymer (CFRP) composites.
7) The various results show that LPBF is a great choice for the fabrication of complex BMG parts, with no required post-processing steps except for surface finishing.

Declaration of Competing Interest

The authors declare that they have no known competing financial interests or personal relationships that could have appeared to influence the work reported in this paper.

Acknowledgment

This work was supported by the "PREcision Additive Manufacturing of Precious metals Alloys (PREAMPA)" project, funded by the Swiss ETH domain within the Strategic Focus Area on Advanced Manufacturing. The generous support of PX Group to the LMTM laboratory is gratefully acknowledged. We also acknowledge the Paul Scherrer Institute, Villigen, Switzerland for provision of synchrotron radiation beamtime at the beamline MS of the Swiss Light Source and thank Dr. Nicola Casati for his assistance.

Appendix A. Supplementary data

Supplementary data to this article can be found online at https://doi.org/10.1016/j.matdes.2020.109400.

References

[1] J.F. Löffler, A.A. Kündig, F.H. Dalla Torre, Rapid solidification and bulk metallic glasses — processing and properties, Mater. Process. Handb, Taylor& Francis Group, New York, 2007.
[2] W.H. Wang, C. Dong, C.H. Shek, Bulk metallic glasses, Mater. Sci. Eng. R. Rep. 44 (2004) 45–89, https://doi.org/10.1016/J.MSER.2004.03.001.
[3] J. Schroers, G. Kumar, T.M. Hodges, S. Chan, T.R. Kyriakides, Bulk metallic glasses for biomedical applications, JOM. 61 (2009) 21–29, https://doi.org/10.1007/s11837-009-0128-1.
[4] A.L. Greer, E. Ma, Bulk metallic glasses: at the cutting edge of metals research, MRS Bull. 32 (2007) 611–619, https://doi.org/10.1557/mrs2007.121.
[5] A. Inoue, N. Nishiyama, New bulk metallic glasses for applications as magnetic-sensing, chemical, and structural materials, MRS Bull. 32 (2007) 651–658, https://doi.org/10.1557/mrs2007.128.
[6] J. Schroers, Processing of bulk metallic glass, Adv. Mater. 22 (2010) 1566–1597, https://doi.org/10.1002/adma.200902776.
[7] S. Cardinal, J.M. Pelletier, M. Eisenbart, U.E. Klotz, Influence of crystallinity on thermo-process ability and mechanical properties in a au-based bulk metallic glass, Mater. Sci. Eng. A 660 (2016) 158–165, https://doi.org/10.1016/j.msea.2016.02.078.
[8] C. Suryanarayana, A. Inoue, Bulk Metallic Glasses, Second ed, 2018 Taylor& Francis Group.
[9] T. Vilaro, V. Kottman-Rexerodt, M. Thomas, C. Colin, P. Bertrand, L. Thivillon, S. Abed, V. Ji, P. Aubry, P. Peyre, T. Malot, Direct Fabrication of a Ti-47Al-2Cr-2Nb Alloy by Selective Laser Melting and Direct Metal Deposition Processes, THERMEC 2009 Suppl, Trans Tech Publications 2010, pp. 586–591, https://doi.org/10.4028/www.scientific.net/AMR.89-91.586.
[10] X.D. Nong, X.L. Zhou, Y.X. Ren, Fabrication and characterization of Fe-based metallic glasses by selective laser melting, Opt. Laser Technol. 109 (2019) 20–26, https://doi.org/10.1016/j.optlastec.2018.07.059.
[11] N. Li, J. Zhang, W. Xing, D. Ouyang, L. Liu, 3D printing of Fe-based bulk metallic glass composites with combined high strength and fracture toughness, Mater. Des. 143 (2018) 285–296, https://doi.org/10.1016/j.matdes.2018.01.061.
[12] H.Y. Jung, S.J. Choi, K.G. Prashanth, M. Stoica, S. Scudino, S. Yi, U. Kühn, D.H. Kim, K.B. Kim, J. Eckert, Fabrication of Fe-based bulk metallic glass by selective laser melting: a parameter study, Mater. Des. 86 (2015) 703–708, https://doi.org/10.1016/j.matdes.2015.07.145.
[13] S. Pauly, L. Löber, R. Petters, M. Stoica, S. Scudino, U. Kühn, J. Eckert, Processing Metallic Glasses by Selective Laser Melting, 2013https://doi.org/10.1016/j.mattod.2013.01.018.
[14] Z. Mahbooba, L. Thorsson, M. Unosson, P. Skoglund, H. West, T. Horn, C. Rock, E. Vogli, O. Harrysson, Additive manufacturing of an iron-based bulk metallic glass larger than the critical casting thickness, Appl. Mater. Today 11 (2018) 264–269, https://doi.org/10.1016/j.apmt.2018.02.011.
[15] D. Ouyang, W. Xing, N. Li, Y. Li, L. Liu, Structural evolutions in 3D-printed Fe-based metallic glass fabricated by selective laser melting, Addit. Manuf. 23 (2018) 246–252, https://doi.org/10.1016/j.addma.2018.08.020.
[16] L. Wang, H. Wang, Y. Liu, Z. Fu, T. Peng, J. Shen, S. Zhou, M. Yan, G. Wang, Y. Dai, Selective laser melting helps fabricate record-large bulk metallic glass: Experiments, simulation and demonstrative part, J. Alloys Compd. 808 (2019)https://doi.org/10.1016/j.jallcom.2019.151731.
[17] D.C. Hofmann, P. Bordeenithikasem, A. Pate, S.N. Roberts, E. Vogli, Developing processing parameters and characterizing microstructure and properties of an additively manufactured FeCrMoBC metallic glass forming alloy, Adv. Eng. Mater. 20 (2018)https://doi.org/10.1002/adem.201800433.
[18] Y.G. Nam, B. Koo, M.S. Chang, S. Yang, J. Yu, Y.H. Park, J.W. Jeong, Selective laser melting vitrification of amorphous soft magnetic alloys with help of double-scanning-induced compositional homogeneity, Mater. Lett. 261 (2020) 127068, https://doi.org/10.1016/j.matlet.2019.127068.
[19] Y.M. Zou, Y.S. Wu, K.F. Li, C.L. Tan, Z.G. Qiu, D.C. Zeng, Selective laser melting of crack-free Fe-based bulk metallic glass via chessboard scanning strategy, Mater. Lett. 272 (2020) 2–5, https://doi.org/10.1016/j.matlet.2020.127824.
[20] K.G. Prashanth, H. Shakur Shahabi, H. Attar, V.C. Srivastava, N. Ellendt, V. Uhlenwinkel, J. Eckert, S. Scudino, Production of high strength Al85Nd8Ni5Co2alloy by selective laser melting, Addit. Manuf. 6 (2015) 1–5, https://doi.org/10.1016/j.addma.2015.01.001.
[21] X.P. Li, M. Roberts, Y.J. Liu, C.W. Kang, H. Huang, T.B. Sercombe, Effect of substrate temperature on the interface bond between support and substrate during selective laser melting of Al-Ni-Y-co-La metallic glass, Mater. Des. 65 (2015) 1–6, https://doi.org/10.1016/j.matdes.2014.08.065.
[22] X.P. Li, C.W. Kang, H. Huang, L.C. Zhang, T.B. Sercombe, Selective laser melting of an $Al_{86}Ni_6Y_{4.5}Co_2La_{1.5}$ metallic glass: Processing, microstructure evolution and mechanical properties, Mater. Sci. Eng. A 606 (2014) 370–379, https://doi.org/10.1016/j.msea.2014.03.097.
[23] X.P. Li, C.W. Kang, H. Huang, T.B. Sercombe, The role of a low-energy-density re-scan in fabricating crack-free $Al_{85}Ni_5Y_6Co_2Fe_2$bulk metallic glass composites via selective laser melting, Mater. Des. 63 (2014) 407–411, https://doi.org/10.1016/j.matdes.2014.06.022.
[24] X.P. Li, M.P. Roberts, S. O'Keeffe, T.B. Sercombe, Selective laser melting of Zr-based bulk metallic glasses: processing, microstructure and mechanical properties, Mater. Des. 112 (2016) 217–226, https://doi.org/10.1016/j.matdes.2016.09.071.
[25] P. Bordeenithikasem, M. Stolpe, A. Elsen, D.C. Hofmann, Glass forming ability, flexural strength, and wear properties of additively manufactured Zr-based bulk metallic glasses produced through laser powder bed fusion, Addit. Manuf. 21 (2018) 312–317, https://doi.org/10.1016/j.addma.2018.03.023.
[26] P. Zhang, D. Ouyang, L. Liu, Enhanced mechanical properties of 3D printed Zr-based BMG composite reinforced with Ta precipitates, J. Alloys Compd. 803 (2019) 476–483, https://doi.org/10.1016/j.jallcom.2019.06.303.
[27] C. Zhang, X. Min Li, S.Q. Liu, H. Liu, L.J. Yu, L. Liu, 3D printing of Zr-based bulk metallic glasses and components for potential biomedical applications, J. Alloys Compd. 790 (2019) 963–973, https://doi.org/10.1016/j.jallcom.2019.03.275.
[28] J.P. Best, J. Ast, B. Li, M. Stolpe, R. Busch, F. Yang, X. Li, J. Michler, J.J. Kruzic, Relating fracture toughness to micro-pillar compression response for a laser powder bed additive manufactured bulk metallic glass, Mater. Sci. Eng. A 770 (2020) 138535, https://doi.org/10.1016/j.msea.2019.138535.
[29] L. Deng, A. Gebert, L. Zhang, H.Y. Chen, D.D. Gu, U. Kühn, M. Zimmermann, K. Kosiba, S. Pauly, Mechanical performance and corrosion behaviour of Zr-based bulk metallic glass produced by selective laser melting, Mater. Des. 189 (2020) 1–11, https://doi.org/10.1016/j.matdes.2020.108532.
[30] D. Ouyang, Q. Zheng, L. Wang, H. Wang, C. Yang, P. Zhang, N. Li, The brittleness of post-treatment of 3D printed Zr-based metallic glasses in supercooled liquid state, Mater. Sci. Eng. A 782 (2020) 139259, https://doi.org/10.1016/j.msea.2020.139259.
[31] Y. Zhang, X. Lin, X. Gao, X. Su, S. Guo, W. Huang, Crystallization behavior of $Zr_{55}Cu_{30}Al_{10}Ni_5$ amorphous alloys produced by selective laser melting of preannealed powders, J. Alloys Compd. 819 (2020) 153013, https://doi.org/10.1016/j.jallcom.2019.153013.
[32] J. Shi, S. Ma, S. Wei, J.P. Best, M. Stolpe, A. Beckmann, S. Mostafavi, S. Korte-Kerzel, B. Markert, 3D pore structure characterization and hardness in a powder bed fusion-processed fully amorphous Zr-based bulk metallic glass, Mater. Charact. 162 (2020) 110178, https://doi.org/10.1016/j.matchar.2020.110178.

[33] S. Pauly, C. Schricker, S. Scudino, L. Deng, U. Kühn, Processing a glass-forming Zr-based alloy by selective laser melting, Mater. Des. 135 (2017) 133–141, https://doi.org/10.1016/j.matdes.2017.08.070.

[34] Y. Lu, H. Zhang, H. Li, H. Xu, G. Huang, Z. Qin, X. Lu, Crystallization prediction on laser three-dimensional printing of Zr-based bulk metallic glass, J. Non-Cryst. Solids 461 (2017) 12–17, https://doi.org/10.1016/j.jnoncrysol.2017.01.038.

[35] D. Ouyang, N. Li, W. Xing, J. Zhang, L. Liu, 3D printing of crack-free high strength Zr-based bulk metallic glass composite by selective laser melting, Intermetallics. 90 (2017) 128–134, https://doi.org/10.1016/j.intermet.2017.07.010.

[36] C. Yang, C. Zhang, W. Xing, L. Liu, 3D printing of Zr-based bulk metallic glasses with complex geometries and enhanced catalytic properties, Intermetallics. 94 (2018) 22–28, https://doi.org/10.1016/j.intermet.2017.12.018.

[37] D. Ouyang, N. Li, L. Liu, Structural heterogeneity in 3D printed Zr-based bulk metallic glass by selective laser melting, J. Alloys Compd. 740 (2018) 603–609, https://doi.org/10.1016/j.jallcom.2018.01.037.

[38] V. Pacheco, D. Karlsson, J.J. Marattukalam, M. Stolpe, B. Hjörvarsson, U. Jansson, M. Sahlberg, Thermal stability and crystallization of a Zr-based metallic glass produced by suction casting and selective laser melting, J. Alloys Compd. 153995 (2019) https://doi.org/10.1016/j.jallcom.2020.153995.

[39] J.J. Marattukalam, V. Pacheco, D. Karlsson, L. Riekehr, J. Lindwall, F. Forsberg, U. Jansson, M. Sahlberg, B. Hjörvarsson, Development of process parameters for selective laser melting of a Zr-based bulk metallic glass, Addit. Manuf. 33 (2020) 101124, https://doi.org/10.1016/j.addma.2020.101124.

[40] N. Sohrabi, R.S. Panikar, J. Jhabvala, A.R. Buch, S. Mischler, R.E. Logé, Laser coating of a Zr-based metallic glass on an aluminum substrate, Surf. Coat. Technol. 400 (2020) https://doi.org/10.1016/j.surfcoat.2020.126223.

[41] L. Deng, S. Wang, P. Wang, U. Kühn, S. Pauly, Selective laser melting of a Ti-based bulk metallic glass, Mater. Lett. 212 (2018) 346–349, https://doi.org/10.1016/j.matlet.2017.10.130.

[42] X. Lu, M. Nursulton, Y. Du, W. Liao, Structural and mechanical characteristics of $Cu_{50}Zr_{43}A_{l7}$ bulk metallic glass fabricated by selective laser melting, Materials (Basel). 12 (2019)https://doi.org/10.3390/ma12050775.

[43] X. Gao, Z. Liu, J. Li, E. Liu, C. Yue, K. Zhao, G. Yang, Selective laser melting of CuZr-based metallic glass composites, Mater. Lett. 259 (2020) 126724, https://doi.org/10.1016/j.matlet.2019.126724.

[44] T. DebRoy, H.L. Wei, J.S. Zuback, T. Mukherjee, J.W. Elmer, J.O. Milewski, A.M. Beese, A. Wilson-Heid, A. De, W. Zhang, Additive manufacturing of metallic components – process, structure and properties, Prog. Mater. Sci. 92 (2018) 112–224, https://doi.org/10.1016/j.pmatsci.2017.10.001.

[45] Y. Li, S.J. Poon, G.J. Shiflet, J. Xu, D.H. Kim, J.F. Löffler, Formation of bulk metallic glasses and their composites, MRS Bull. 32 (2007) 624–628, https://doi.org/10.1557/mrs2007.123.

[46] J.F. Löffler, Bulk metallic glasses, Intermetallics. 11 (2003) 529–540, https://doi.org/10.1016/S0966-9795(03)00046-3.

[47] J. Lindwall, V. Pacheco, M. Sahlberg, A. Lundbäck, L.E. Lindgren, Thermal simulation and phase modeling of bulk metallic glass in the powder bed fusion process, Addit. Manuf. 27 (2019) 345–352, https://doi.org/10.1016/j.addma.2019.03.011.

[48] J.P. Best, H.E. Ostergaard, B. Li, M. Stolpe, F. Yang, K. Nomoto, M.T. Hasib, O. Muránsky, R. Busch, X. Li, J.J. Kruzic, Fracture and fatigue behaviour of a laser additive manufactured Zr-based bulk metallic glass, Addit. Manuf. 36 (2020) 101416, https://doi.org/10.1016/j.addma.2020.101416.

[49] L. Rebaioli, I. Fassi, A review on benchmark artifacts for evaluating the geometrical performance of additive manufacturing processes, Int. J. Adv. Manuf. Technol. 93 (2017) 2571–2598, https://doi.org/10.1007/s00170-017-0570-0.

[50] J.P. Kruth, Vandenbroucke, J. Van Vaerenbergh, P. Mercelis, Benchmarking of different SLS/SLM processes as rapid manufacturing techniques, Proc. Int. Conf. Polym. Mould. Innov. PMI 2005, Gent, Belgium 2005, p. 4, https://doi.org/10.1186/s13036-015-0001-4.

[51] M. Mahesh, Y.S. Wong, J.Y.H. Fuh, H.T. Loh, Benchmarking for comparative evaluation of RP systems and processes, Rapid Prototyp. J. 10 (2004) 123–135, https://doi.org/10.1108/13552540410526999.

[52] J. Ilčík, D. Koutny, D. Paloušek, Geometrical accuracy of the metal parts produced by selective laser melting: initial tests, Mod. Methods Constr 2014, pp. 573–582, https://doi.org/10.1007/978-3-319-05203-8_76.

[53] P. Kruth, Jean-Pierre, Ben Vandenbroucke, Van Vaerenbergh, Jonas, Mercelis, Benchmarking of different SLS/SLM processes as rapid manufacturing techniques, Proc. Int. Conf. Polym. \& Mould. Innov. PMI 20052005 p. paper 525.

[54] P.R. Willmott, D. Meister, S.J. Leake, M. Lange, A. Bergamaschi, M. Böge, M. Calvi, C. Cancellieri, N. Casati, A. Cervellino, Q. Chen, C. David, U. Flechsig, F. Gozzo, B. Henrich, S. Jäggi-Spielmann, B. Jakob, I. Kalichava, P. Karvinen, J. Krempasky, A. Lüdeke, R. Lüscher, S. Maag, C. Quitmann, M.L. Reinle-Schmitt, T. Schmidt, B. Schmitt, A. Streun, I. Vartiainen, M. Vitins, X. Wang, R. Wullschleger, The materials science beamline upgrade at the swiss light source, J. Synchrotron Radiat. 20 (2013) 667–682, https://doi.org/10.1107/S0909049513018475.

[55] C. Prescher, V.B. Prakapenka, DIOPTAS: a program for reduction of two-dimensional X-ray diffraction data and data exploration, High Pressure Res. 35 (2015) 223–230, https://doi.org/10.1080/08957959.2015.1059835.

[56] V. Dyadkin, P. Pattison, V. Dmitriev, D. Chernyshov, A new multipurpose diffractometer PILATUS@SNBL, J. Synchrotron Radiat. 23 (2016) 825–829, https://doi.org/10.1107/S1600577516002411.

[57] J. Stojadinovic, D. Bouvet, M. Declercq, S. Mischler, Influence of chelating agents on the tribocorrosion of tungsten in sulphuric acid solution, Electrochim. Acta 56 (2011) 7131–7140, https://doi.org/10.1016/J.ELECTACTA.2011.05.084.

[58] A.A. Kündig, M. Ohnuma, T. Ohkubo, K. Hono, Early crystallization stages in a Zr–Cu–Ni–Al–Ti metallic glass, Acta Mater. 53 (2005) 2091–2099, https://doi.org/10.1016/j.actamat.2005.01.022.

[59] K. Kajiwara, M. Ohnuma, T. Ohkubo, D.H. Ping, K. Hono, APFIM/TEM/SAXS studies of early stage crystallization of a $Zr_{52.5}Cu_{17.9}Ni_{14.6}Al_{10}Ti_5$ metallic glass, Mater. Sci. Eng. A 375–377 (2004) 738–743, https://doi.org/10.1016/j.msea.2003.10.087.

[60] M. Baricco, S. Spriano, I. Chang, M.I. Petrzhik, L. Battezzati, "Big cube" phase formation in Zr-based metallic glasses, Mater. Sci. Eng. A 304–306 (2001) 305–310, https://doi.org/10.1016/S0921-5093(00)01438-6.

[61] A. Ericsson, V. Pacheco, M. Sahlberg, J. Lindwall, H. Hallberg, M. Fisk, Transient nucleation in selective laser melting of Zr-based bulk metallic glass, Mater. Des. 195 (2020) 108958, https://doi.org/10.1016/j.matdes.2020.108958.

[62] G. Yang, X. Lin, F. Liu, Q. Hu, L. Ma, J. Li, W. Huang, Laser solid forming Zr-based bulk metallic glass, Intermetallics. 22 (2012) 110–115, https://doi.org/10.1016/j.intermet.2011.10.008.

[63] Y. Shen, Y. Li, C. Chen, H.L. Tsai, 3D printing of large, complex metallic glass structures, Mater. Des. 117 (2017) 213–222, https://doi.org/10.1016/j.matdes.2016.12.087.

[64] Y. Lu, Y. Huang, J. Wu, X. Lu, Z. Qin, D. Daisenberger, Y.L. Chiu, Graded structure of laser direct manufacturing bulk metallic glass, Intermetallics. 103 (2018) 67–71, https://doi.org/10.1016/j.intermet.2018.10.005.

[65] H.D. Vora, S. Mridha, S. Katakam, H.S. Arora, S. Mukherjee, N.B. Dahotre, Thermodynamics and kinetics of laser induced transformation in zirconium based bulk metallic glass, J. Non-Cryst. Solids 432 (2016) 237–245, https://doi.org/10.1016/j.jnoncrysol.2015.10.013.

[66] Y. Zhang, X. Lin, L. Wang, L. Wei, F. Liu, W. Huang, Microstructural analysis of $Zr_{55}Cu_{30}Al_{10}Ni_5$ bulk metallic glasses by laser surface remelting and laser solid forming, Intermetallics. 66 (2015) 22–30, https://doi.org/10.1016/j.intermet.2015.06.007.

[67] S. Kolossov, Non-linear Model and Finite Element Simulation of the Selective Laser Sintering Process, EPFL 2005https://doi.org/10.5075/epfl-thesis-3178.

[68] H. Ghasemi-Tabasi, J. Jhabvala, E. Boillat, T. Ivas, R. Drissi-Daoudi, R.E. Logé, An effective rule for translating optimal selective laser melting processing parameters from one material to another, Addit. Manuf. 36 (2020) 101496, https://doi.org/10.1016/j.addma.2020.101496.

[69] Y. Shen, Y. Li, H.L. Tsai, Effect of pre-existing nuclei on crystallization during laser welding of Zr-based metallic glass, J. Non-Cryst. Solids 513 (2019) 55–63, https://doi.org/10.1016/j.jnoncrysol.2019.03.022.

[70] B. Bochtler, M. Stolpe, B. Reiplinger, R. Busch, Consolidation of amorphous powder by thermoplastic forming and subsequent mechanical testing, Mater. Des. 140 (2018) 188–195, https://doi.org/10.1016/j.matdes.2017.11.058.

[71] Standard Test Methods for Flexural Properties of Unreinforced and Reinforced Plastics and Electrical Insulating Materials2017https://doi.org/10.1520/D0790-17.

[72] S. Romano, A. Brückner-Foit, A. Brandão, J. Gumpinger, T. Ghidini, S. Beretta, Fatigue properties of AlSi10Mg obtained by additive manufacturing: Defect-based modelling and prediction of fatigue strength, Eng. Fract. Mech. 187 (2018) 165–189, https://doi.org/10.1016/j.engfracmech.2017.11.002.

[73] C.A. Schuh, T.C. Hufnagel, U. Ramamurty, Mechanical behavior of amorphous alloys, Acta Mater. 55 (2007) 4067–4109, https://doi.org/10.1016/J.ACTAMAT.2007.01.052.

[74] R. Maaß, J.F. Löffler, Shear-band dynamics in metallic glasses, Adv. Funct. Mater. 25 (2015) 2353–2368, https://doi.org/10.1002/adfm.201404223.

[75] D. Klaumünzer, R. Maaß, J.F. Löffler, Stick-slip dynamics and recent insights into shear banding in metallic glasses, J. Mater. Res. 26 (2011) 1453–1463, https://doi.org/10.1557/jmr.2011.178.

[76] F.H. Dalla Torre, A. Dubach, J. Schällibaum, J.F. Löffler, Shear striations and deformation kinetics in highly deformed Zr-based bulk metallic glasses, Acta Mater. 56 (2008) 4635–4646, https://doi.org/10.1016/j.actamat.2008.05.021.

[77] H.A. Bruck, A.J. Rosakis, W.L. Johnson, The dynamic compressive behavior of beryllium bearing bulk metallic glasses, J. Mater. Res. 11 (1996) 503–511, https://doi.org/10.1557/JMR.1996.0060.

[78] C.T. Liu, L. Heatherly, J.A. Horton, D.S. Easton, C.A. Carmichael, J.L. Wright, J.H. Schneibel, M.H. Yoo, C.H. Chen, A. Inoue, Test environments and mechanical properties of Zr-base bulk amorphous alloys, Metall. Mater. Trans. A. 29 (1998) 1811–1820, https://doi.org/10.1007/s11661-998-0004-6.

[79] M.F. Ashby, Materials Selection in Mechanical Design, Second Edi, Butterworth-Heinemann, Oxford, 1999https://doi.org/10.1017/CBO9781107415324.004.

[80] X. Ji, S. Alavi, S. Harimkar, Dry sliding wear behavior of spark plasma sintered Fe-based bulk metallic glass/graphite composites, Technologies. 4 (2016) 27, https://doi.org/10.3390/technologies4030027.

[81] X.X. Li, Y. Zhou, X.L. Ji, Y.X. Li, S.Q. Wang, Effects of sliding velocity on tribo-oxides and wear behavior of Ti-6Al-4V alloy, Tribol. Int. 91 (2015) 228–234, https://doi.org/10.1016/j.triboint.2015.02.009.

[82] D. Das, A.K. Dutta, K.K. Ray, On the enhancement of wear resistance of tool steels by cryogenic treatment, Philos. Mag. Lett. 88 (2008) 801–811, https://doi.org/10.1080/09500830802380788.

[83] Y. Lu, G. Huang, Y. Wang, H. Li, Z. Qin, X. Lu, Crack-free Fe-based amorphous coating synthesized by laser cladding, Mater. Lett. 210 (2018) 46–50, https://doi.org/10.1016/j.matlet.2017.08.125.

[84] J. Schroers, The superplastic forming of bulk metallic glass, JOM. 57 (2005) 35–39.

[85] Y. Tian, D. Tomus, P. Rometsch, X. Wu, Influences of processing parameters on surface roughness of Hastelloy X produced by selective laser melting, Addit. Manuf. 13 (2017) 103–112, https://doi.org/10.1016/j.addma.2016.10.010.

[86] G. Strano, L. Hao, R.M. Everson, K.E. Evans, Surface roughness analysis, modelling and prediction in selective laser melting, J. Mater. Process. Technol. 213 (2013) 589–597, https://doi.org/10.1016/j.jmatprotec.2012.11.011.